

## Detergent Foam Images as Analogue/Digital Model Fluids. 2. Investigation of Neighborhood Partition of the Radial Distribution Function

Daniel J. Graham,\* Peter Magdalinos,<sup>†</sup> and Dante Pimentel

Department of Chemistry, Loyola University of Chicago, Chicago, Illinois 60626

Received: December 9, 1996; In Final Form: July 9, 1997<sup>®</sup>

Investigation continues of detergent foam images as analogue/digital (A/D) model fluids. Attention turns to the radial distribution function  $G(r)$  and how it is partitioned in terms of individual neighborhoods: first, second, third, etc. Data are illustrated for liquid- and gaslike systems, and key features of the neighborhood partition are enumerated. Data are compared with mathematical constructs offered by the ideal gas, hard disk, and hexagonal crystalline models. Such comparison points to an indirect method for partitioning  $G(r)$  into neighborhood distributions in agreement with experiment. Notably, the method requires no specification of particle shapes and potentials. The indirect method is applied to liquid sodium using X-ray data of previous researchers. Structures of liquid sodium are offered via an alternative, empirical way.

### I. Introduction

The radial distribution function  $G(r)$  for a monatomic fluid demonstrates three distinct regions: (1) close to the origin corresponding to excluded and free volume about the reference particle, (2) hills and valleys allied with shells about the reference particle, and (3) the region corresponding to atoms whose precise configuration does not hinge upon the reference particle. These features are shown in Figure 1 for a generic liquid and interacting gas.<sup>1</sup> For real materials (lithium, sodium, etc.), all  $G(r)$  details follow from diffraction experiments using X-rays or neutrons.<sup>2</sup>

$G(r)$  can be explained entirely in terms of atom pair correlations. Yet how it is partitioned into subsets of neighborhoods (first, second, third, etc.) is never revealed in the scattering data of origin. For this reason, the structure content in  $G(r)$  is not without ambiguity. In turn, there are many questions which go unanswered on an experimental basis. For example, how is a fluid's structure related to the crystalline phase? To what degree does a liquid mimic a perturbed crystal? What properties of neighborhood subsets of  $G(r)$  transcend the phase under consideration? What mathematical constructs offer an accurate description of neighborhoods embedded in  $G(r)$ ?

Because of limitations in the lab, computer simulations offer the most immediate ways to tackle problems such as the above. By programming reasonable assumptions about atom sizes and potentials, reasonable facsimiles of fluids can be constructed. Indeed, "particles" of a virtual fluid can be tracked to very high precision, as is accomplished routinely by Monte Carlo (MC) and molecular dynamics (MD) programs.<sup>3</sup> Many quantities which are impossible to obtain in lab experiments can thus be realized quite easily in virtual space. Neighborhood distributions embedded in  $G(r)$  are only one example. In a complementary way, mathematical models such as hard sphere address the physics of fluids at the atomic level.<sup>4</sup> This sets the stage for additional computer experiments with extrapolation to real materials.<sup>5</sup>

The previous paper described an alternative way to model fluids using detergent foam images.<sup>6</sup> While certain limitations

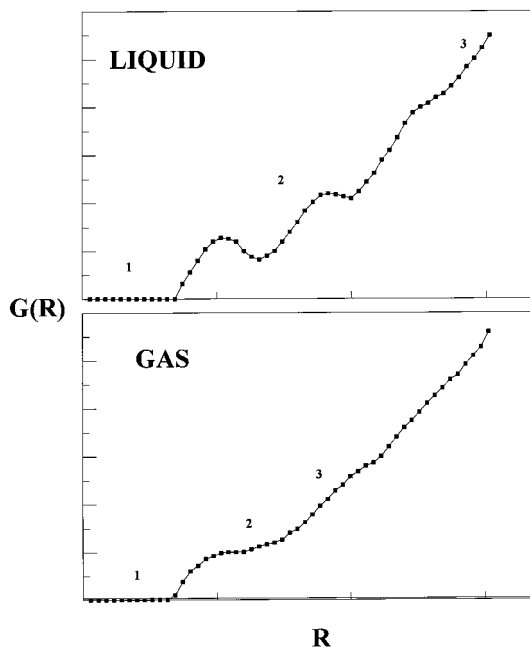


**Figure 1.** Radial distribution functions for generic monatomic liquid and gas. Numbers refer to regions discussed in text.

are confronted in terms of sample dimensionality, other features invite further exploration. Most notably, in this approach all structures originate from real materials on a lab benchtop. The "analogue" (A) component ensures that the "particles" (atom icons dressed on plateau border vertexes) are centered by nature's exact potentials. Unlike MC and MD simulations, no assumptions are required about pairwise additivity. At the same time, the model's "digital" (D) component means that several thousand particles can be easily accommodated. Phase signatures, correlation functions, and thermodynamic quantities are among the products of this model.<sup>6</sup> These are available on a particlewise basis, much as in MC and MD simulations.

This paper further examines what A/D models offer about fluid structure at the atomic level. Attention thus turns to points raised in the second paragraph, namely how  $G(r)$  is partitioned into discrete neighborhoods. Overall, the purpose here will be to *apply* the model, using technical machinery offered in the previous study. This seems both timely and interesting, for the

\* To whom all correspondence should be addressed. Fax (773) 508-3086; E-mail DGRAHA1@LUC.EDU.

<sup>†</sup> Present address: Department of Chemistry, Northern Illinois University, DeKalb, IL 60115.

<sup>®</sup> Abstract published in *Advance ACS Abstracts*, December 1, 1997.

results offer a basis to address the above questions, with applications to real fluids.

The organization will be as follows. In section II, an overview of the neighborhood partition of  $G(r)$  will be presented. Reference will be made to theory by previous researchers. The experimental procedure will be reviewed briefly in section III, the details having been given in the previous paper. Experimental results will then be illustrated in section IV for typical liquid- and gaslike systems. In so doing, key characteristics of the neighborhood partition will be established. Also in section IV, comparison will be made between experimental data and the mathematical constructs of section II. This points to an indirect method of extracting neighborhood distributions from  $G(r)$  in good agreement with experiment. Section V is devoted to discussion of the results and their significance. As the model pair potentials are most akin to those of alkali metals (cf. previous paper), the indirect method is applied to liquid sodium. The application offers fluid structures at a level of detail unobtainable by diffraction data alone.

## II. Neighborhood Partition of $G(r)$ : Mathematical Considerations

For a 2D monodisperse fluid of  $N$  particles,  $G(r) = 2\pi\rho r g(r)$  ( $4\pi\rho r^2 g(r)$  in 3D) and can be expressed as a sum of neighborhood distribution functions:

$$G(r) = P(1,r) + P(2,r) + \dots + P(n,r) + \dots + P(N-1,r) \\ = \sum_{n=1}^{n=N-1} P(n,r) \quad (1)$$

In this section, conventional notation is followed whereby  $g(r)$ ,  $\rho$ ,  $r$ , and  $P(n,r)$  respectively refer to the pair correlation function, number density, radial distance, and distribution function for the  $n$ th nearest neighbor of the reference particle. As is well-known,  $G(r) dr$  measures the probability of finding any neighboring particle at a distance bounded by  $r$  and  $r + dr$ . By analogy,  $P(n,r) dr$  is the probability of observing the  $n$ th neighbor of the reference particle in the same interval.

For eq 1 to hold, normalization is required for each rhs function, namely

$$\int_0^\infty P(n,r) dr = 1 \quad (2)$$

This condition lends itself to average values (moments) affiliated with each of the  $P(n,r)$ , for example the distance of the  $n$ th nearest neighbor from the reference particle:

$$\langle r_n \rangle = \int_0^\infty dr P(n,r) \quad (3)$$

Of course, lab experiments fall way short of providing  $P(n,r)$  and moments for arbitrary  $n$ . How can the rhs functions in eq 1 be specified when fluid diffraction data yield only their summation?

Theory by a number of researchers has grappled with these issues, especially concerning  $P(1,r)$ . This more or less began with Hertz, who established  $P(1,r)$  for an ideal gas.<sup>7</sup> Years later, a model for  $P(1,r)$  was a central component of the scaled particle theory by Reiss, Frisch, and Lebowitz.<sup>8</sup> More recently, Torquato, Lu, and Rubinstein established  $P(1,r)$  for fluids operating under a variety of geometrical constraints.<sup>9</sup> MacDonald has also addressed first neighborhood properties of one, two, and three dimensions.<sup>10</sup>

For the totality of neighborhoods, Mazur has derived expressions for hard sphere systems, making use of an excluded area

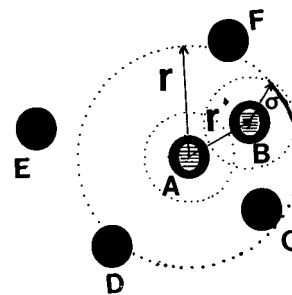


**Figure 2.** Hard disks confined to a plane. The intersection between the exclusion zone around particle **B** and a circle of radius  $r$  about reference particle **A** is accented by blackening. This length is designated  $L_o(r,r')$  as discussed in the text.

approximation. His approach is readily adapted to the 2D situation, namely hard circular disks scattered on a plane. This adaptation is sketched here, as it offers a first, reference picture of neighborhood distributions for a 2D disordered phase.

In the limit of zero particle density, it is readily shown that

$$P(1,r) = G(r) \exp[-\int_0^r dr' G(r')] \quad (4)$$

For a 2D ideal gas,  $P(1,r)$  then assumes an especially compact form, given that  $g(r) = 1$ . One obtains by substitution and integration

$$P(1,r) = 2\pi\rho r \exp[-\pi r^2 \rho] \quad (5)$$

Equation 5 is basically the 2D analogue of Hertz's result in 3D, namely  $P(1,r) = 4\pi r^2 \rho \exp[-4\pi r^3 \rho/3]$ . To calculate  $P(n,r)$  for  $n > 1$  in the limit of zero density, the following algorithm can then be used:

$$P(n,r) = \{G(r) - \sum_{m=1}^{n-1} P(m,r)\} \times \\ \exp\{-\int_0^r dr' [G(r') - \sum_{m=1}^{n-1} P(m,r')]\} \quad (6)$$

The case of hard disks on a plane is constructed (following Mazur) by looking at  $G(r)$  in relation to  $G(r|0)$ , the conditional probability for finding a neighbor at  $r$ , when there is no neighbor closer than  $r$ . A key idea here is that there will be a circular exclusion plane of radius  $\sigma$ . Figure 2 shows how the centers of all neighboring particles (disks) can never be within a prescribed zone about reference **A**. The zone about any neighbor **B** then affects the probability of observing other disks **C**, **D**, etc., on circles inscribed about the reference particle.

Toward obtaining  $G(r|0)$ , one needs to compute the length of intersection between the exclusion zone around **B** and a circle of radius  $r$  inscribed about **A**. This length is designated  $L_o(r,r')$  (by analogy with surface area  $A_o(r,r')$  in Mazur's work), where  $r'$  is the distance along the line between the **A**,**B** centers. The following expressions then account for all possibilities regarding the relative placement of particles:

$$L_o(r,r') = 0 \quad \text{for } r' > (r + \sigma) \quad \text{or } r' < (r - \sigma)$$

$$L_o(r,r') = 2r\Theta \quad \text{for } r' < (r + \sigma) \quad \text{or } r' > (r - \sigma) \quad (7)$$

where

$$\Theta = \arccos \frac{(r^2 + r'^2 - \sigma^2)}{2rr'} \quad (8)$$

Note that an average value of  $L_o(r, r')$  is obtained by integration:

$$\begin{aligned}\langle L_o(r, r') \rangle &= \int_0^r dr' L_o(r, r') G(r') \\ &= L_{ex}(r)\end{aligned}\quad (9)$$

The subscript “ex” emphasizes the exclusion of particles from the arc region highlighted in Figure 2.

By the above, one is led to  $G(r|0)$  as a corrected version of  $G(r)$ , namely

$$G(r|0) = G(r)[1 + L_{ex}(r)/2\pi r] \quad (10)$$

An expression for  $P(1, r)$  then follows by analogy with eq 4:

$$P(1, r) = G(r|0) \exp[-\int_0^r dr' G(r'|0)] \quad (11)$$

The overall premise of eqs 7–11 is that particle shape, size, and texture are taken explicitly into account, unlike the case of an ideal gas. The mathematics is tractable, given the geometrical and textural simplicity of hard circular disks on a plane.

By extension,  $G(r|n-1)$  is the probability for finding a neighboring disk at  $r$  when there are  $n-1$  neighbors between  $\sigma$  and  $r$ . An algorithm analogous to eq 6 then leads to all the higher order  $P(n, r)$ . The relevant expressions are

$$\begin{aligned}G(r|n-1) &= [G(r) - \sum_{m=1}^{n-1} P(r, m)] \times \\ &\quad \frac{\{1 + \int_{\sigma}^r dr' [G(r') - \sum_{m=1}^{n-1} P(r', m)] L_o(r, r')\}}{2\pi r}\end{aligned}\quad (12)$$

and

$$P(n, r) = G(r|n-1) \exp[-\int_0^r dr' G(r'|n-1)] \quad (13)$$

Now in the A/D model at hand, the “particles” will be specified by Gaussian functions; as such, there is no strict conformation to hard disk physics. Yet the mathematics of this section offers a first vehicle for comparing theory with  $P(n, r)$  data obtained in a laboratory, a luxury not obliged by real atomic fluids. This exercise proves of value: it points to an *indirect method* for partitioning fluid  $G(r)$  using parametrized versions of eqs 12 and 13. In the authors’ experience, this method succeeds well with all model results to date, having benefited from the groundwork laid by previous researchers. As we will see, the indirect method sidesteps all specifics about particle shapes and potentials. For this reason, it invites further application (as is done in section V) to real atomic fluids.

### III. Experimental Section

The procedures used for foam sample preparation, image processing, and data analysis were described in the previous paper.<sup>6</sup> Briefly, the experiments were confined to binary aqueous solutions mixed with trapped gas under closed, fixed-temperature conditions. An extended database was established using distilled water, sodium dodecyl sulfate (SDS), and air mixtures. The SDS concentrations fell in the range 0.05–0.13 M. The samples were contained by plexiglass plates (24 × 30 cm<sup>2</sup>). These plates were held at a fixed, uniform separation of ca. 0.15 cm by O-rings (0.5 cm diameter) and epoxy sealant.

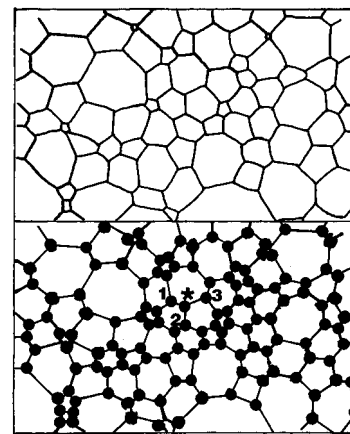


**Figure 3.** Detergent foam and icons. The tagged particle in the icon map is indicated by an asterisk, while the three immediate neighbors are ranked in the order of increasing distance away.

In acquiring image data, a flatbed scanner (HP Deskscan II) and Pentium PC (Gateway) were used. This enabled foam images to be captured in a Windows 3.0 bitmap format, allowing a spatial resolution of ca. 0.02 mm. In establishing icon maps for each data file, plateau vertexes were identified and their center-of-mass positions were treated with Gaussian spatial functions. The Gaussian widths were fixed uniformly in the model fluids by computer software. This ensured monodispersity in each model fluid sample.

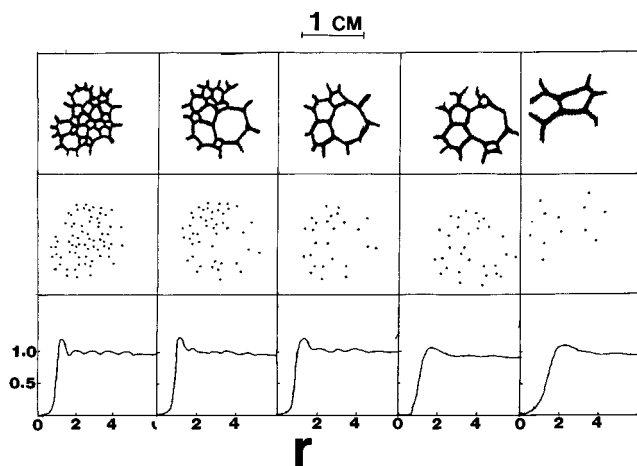
In measuring  $P(n, r)$ , each “atom” (Gaussian icon) was tagged while all its neighbors within a circle of radius of ca. 7 mm were tabulated. The separation between the reference particle and each neighbor was computed and assigned a rank in the order of increasing distance. Gaussian functions were then integrated, the results of which were accumulated in individual arrays. For each icon map, multiple arrays were acquired, one for each neighborhood index  $n = 1, 2, 3, \dots$ . Internally, the array slots were labeled according to radial increments  $\Delta r$ . These slots were used to store the experimental values of  $P(n, r)$ .

Figure 3 illustrates the above concepts by way of a foam shadow image and its corresponding icon map. One “atom” in the lower panel has been tagged (asterisk), while its three immediate neighbors have been ranked (assigned integers) in the order of increasing distance. In this work, the placement of up to 70 neighbors of the tagged particle was investigated. Note that there are no problems in cases of “ties”, i.e.,  $>1$  neighbor at equal distance from the tagged particle. In such cases, one particle is arbitrarily allied with integer  $n$ ; the other(s),  $(n + 1)$ ,  $(n + 2)$ , etc. In all data processing, 486DX and Pentium PCs (Compaq 50 MHz and Gateway 120 MHz, respectively) were used.

For conciseness, discussion will be confined to samples representative of the water/SDS/air database. Specifically, results which establish the essential features of liquid- and gaslike morphologies will be illustrated. The most important properties of the neighborhood partition of  $G(r)$  are contained in these data.

### IV. Results

The top panels of Figure 4 show a portion of a typical foam sample at several stages of coarsening. The top and middle panels, respectively, illustrate the plateau borders and their vertex center-of-mass positions. The lower panels show  $g(r)$  (pair correlation functions) measured for the extended icon maps. The number density decreases on going from left to right, beginning at about 60 particles/cm<sup>2</sup>. Note how  $g(r)$  evinces liquidlike



**Figure 4.** Detergent foam at different coarsening stages. The upper and middle panels, respectively, illustrate the plateau borders and their vertex center-of-mass positions. The lower panels illustrate  $g(r)$ ; numbers along the horizontal axes refer to radial distance in millimeters.

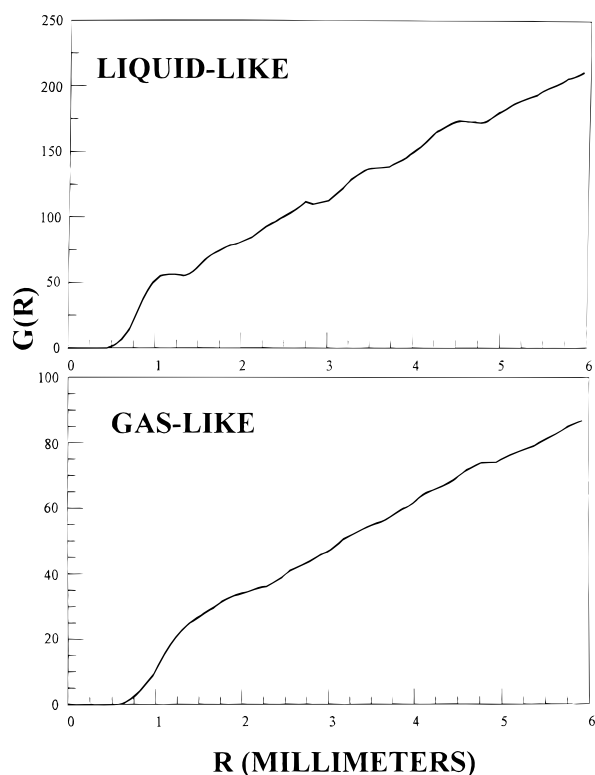


**Figure 5.** Radial distribution of particles for liquid- and gaslike samples. Note the functional similarities between the model data and generic  $G(r)$  of Figure 1.

characteristics in the leftmost (early stage) samples, becoming more gaslike in the lower density cases. This interpretation follows simply from observing the extent of hills and valleys (experimentally significant correlations).

Figure 5 then illustrates the radial distribution function  $G(r)$  for typical liquid- and gaslike samples. In turn, Figure 6 details  $P(n,r)$  embedded in  $G(r)$  for  $n$  as high as 30. For both liquid- and gaslike cases, the neighborhood distributions are single mode, the widths generally increasing with increasing  $n$ . Not surprisingly,  $P(n,r)$  widths are greater for the gaslike samples, compared with liquidlike. In both cases, neighborhood distributions overlap over an extended range of  $n$  values. For example, in the liquid case (upper panel) there is measurable overlap between  $P(1,r)$  and  $P(n,r)$  with  $n$  as high as 12. Such overlap is especially pronounced among the higher order  $P(n,r)$  distributions.

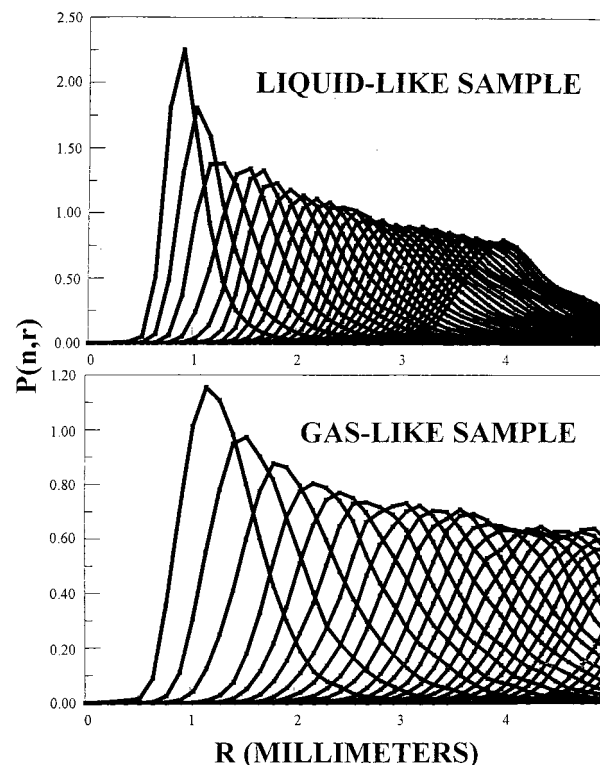


**Figure 6.** Neighborhood distributions measured for liquid- and gaslike samples. Upper and lower panels illustrate  $P(n,r)$ ,  $n = 1, 2, \dots, 30$  allied with  $G(r)$  of Figure 5.

Figures 7 illustrates moment data for the neighborhood distributions; filled squares and circles refer to liquid- and gaslike samples, respectively. The top and middle panels graph  $\langle r_n \rangle$  (first moment) and  $\Sigma_n = (\langle r_n^2 \rangle - \langle r_n \rangle^2)^{1/2}$  (square root of the second moment) as functions of  $n$ . The data show  $\langle r_n \rangle$  (top panel) for both liquid- and gaslike cases to scale with  $n$  according to a fractional exponent. Additional graphing (log-log plots) show the exponents to always be in the range 0.62–0.66, regardless of phase signature. By contrast, one finds  $\Sigma_n$  scaling characteristics (middle panel) to be not so straightforward. For example, the liquidlike case always demonstrates a slight cleft in  $\Sigma_n$  near  $n = 5$ –6.

In the bottom panel of Figure 7, ratios  $\Lambda_n = \langle r_n \rangle / \Sigma_n$  have been plotted versus  $n$ . For liquidlike samples,  $\Lambda_n$  always demonstrates a rise at  $n < 4$ , with a maximum at  $n = 4$ –5, followed by a sharp decline and leveling. By contrast,  $\Lambda_n$  for gaslike samples always have the maximum value at  $n = 1$  and decline exponentially with  $n$ . The top panel of Figure 7 includes  $\langle r_n \rangle$  appropriate to a regular hexagonal lattice, as for a crystalline bubble lattice.<sup>11</sup> One thereby finds few, if any, similarities in the first moment structure of fluid and crystalline samples. In constructing “staircase” plots such as in the upper panel, the lattice constant has been set equal to  $\langle r_{n=1} \rangle$ .

Figure 8 portrays the neighborhood overlaps via  $n \times n$  contour-fill plots. Here the blackness in each slot of the upper triangle arrays (lower triangle parts have been purposely left blank, as entries offer no new information) has been scaled in proportion to the integral:

$$O_{n,n'} = \int dr P(n,r) P(n',r) \quad (14)$$

One observes the plots to demonstrate distinctive “smear” patterns, with the overlap density greatest along the diagonal elements. The density decreases more rapidly along the diagonal for the liquidlike samples, compared with gaslike. Note that for both cases  $O_{n,n+m}$  is roughly equal to  $O_{n' \neq n, n'+m}$ . It is

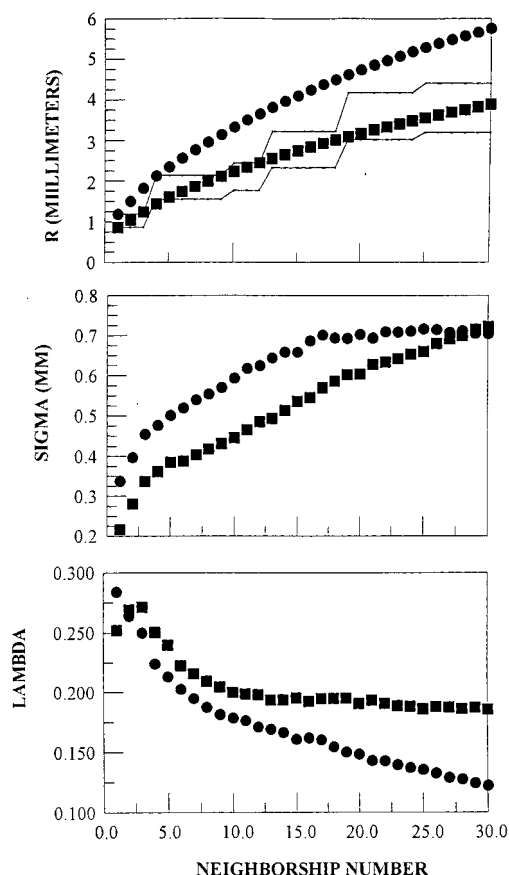


**Figure 7.** Moment data for experimental  $P(n,r)$ . The top, middle, and bottom panels plot  $\langle r_n \rangle$ ,  $\Sigma_n = (\langle r_n^2 \rangle - \langle r_n \rangle^2)^{1/2}$ , and  $\Lambda_n$  as defined in text. The top panel includes staircase plots appropriate to a regular hexagonal lattice. The liquid- and gaslike data are denoted by filled squares and circles, respectively.

this characteristic which elicits a type of “band structure” in the contour-fill plots. This structure is not apparent in the parent data such as in Figure 6. For comparison, Figure 8 includes results appropriate to a regular hexagonal lattice. Again, one notices few if any similarities between fluid and crystalline structures. In particular, the overlap density is concentrated in distinct shells for the crystalline case. For fluid samples, this type of structure is smeared in a strikingly different way.

Experimental data are readily compared with the mathematical constructs of section II. Figure 9 shows the first four neighborships for liquid- and gaslike cases. Filled squares trace experimental  $P(n,r)$ , while the stars denote results of applying eqs 12 and 13 to experimental  $G(r)$  (open squares are discussed below). In relating section II equations to experiment,  $\sigma$  was taken to be a parameter, the value of which minimized deviations between calculated and measured  $P(1,r)$ . The results are that one always finds significant agreement between experiment and calculated for the first neighborship function, especially near the rise and center portions. The more prominent deviations are found in the tail region at higher  $r$ . However, favorable comparisons end here, as there are marked deviations observed for  $P(n,r)$ ,  $n > 1$ . Moment data such as in Figure 11 (filled squares and stars denote experiment and calculated, respectively; open squares again are addressed below) only accentuate these observations. About the only point of accord between experiment and calculated lies in the  $\langle r_n \rangle$  scaling: for both the A/D and hard disk models,  $\langle r_n \rangle$  scales approximately as  $n^{0.65}$ .

On comparing mathematical constructs with model data, one appreciates how sensitive  $P(n,r)$  predictions can be to the choice

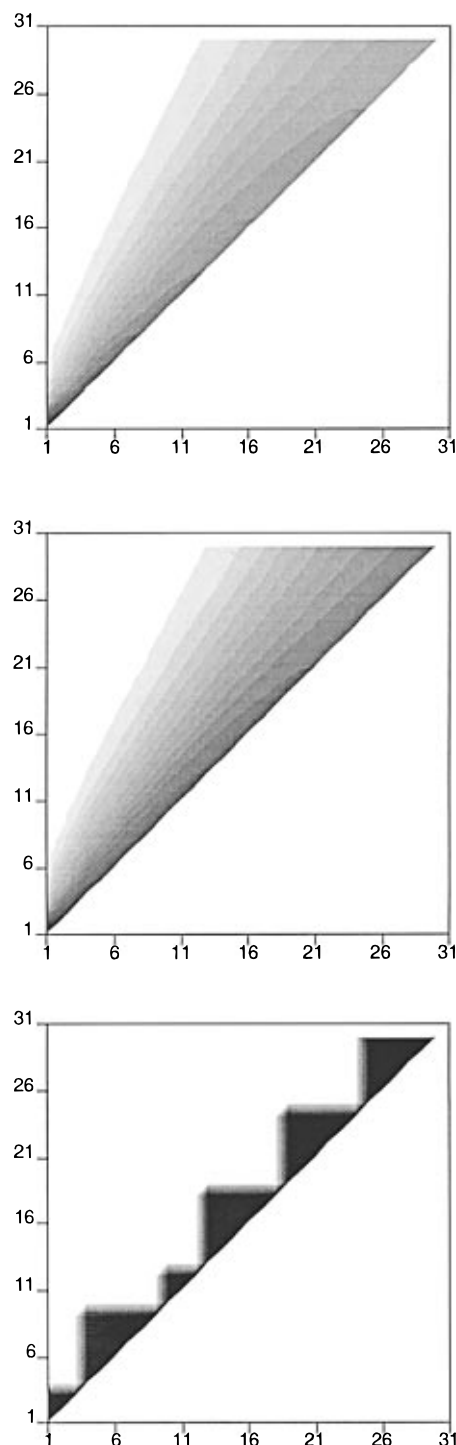


**Figure 8.** Overlap contour-fill plots. Blackness in each slot of the upper triangular arrays has been scaled in proportion to experimental evaluation of eq 14. Uppermost and lowermost plots are allied with liquid- and gaslike samples, respectively. The lowermost plot is for a regular hexagonal lattice; the  $P(n,r)$  were taken to be Gaussian functions with a narrow uniform width. For all three plots, lower triangular portions have been left blank purposely. All three plots employ equal numbers of contours/shading scales.

of particle shapes and potentials. Such appreciation is, by itself, not very significant. Yet for us, this was a key to figuring out a means of constructing good facsimiles of experimental  $P(n,r)$  using  $G(r)$  as the solitary input. In particular, an indirect method of partitioning experimental  $G(r)$  was discovered by parametrizing two of the section II equations and applying them in a stepwise, minimization format. By expressing the neighborhood distributions as  $P(n,r,\lambda_n)$ ,

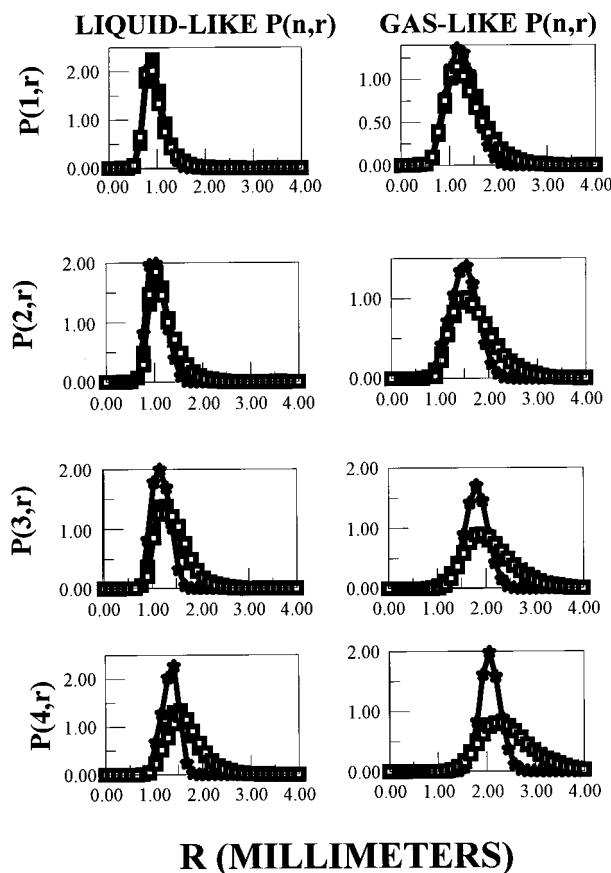


**Figure 9.** Experimental and calculated  $P(n,r)$ . Filled squares trace experimental  $P(n,r)$ , while stars denote results of eqs 12 and 13 applied to  $G(r)$ . Open squares denote results of applying the indirect method to experimental  $G(r)$ .

$$P(n,r,\lambda_n) = a_n \left( G(r) - \sum_{m=1}^{m=n-1} P(m,r,\lambda_m) \right) \times \exp \left[ -\lambda_n \int_0^r dr' (G(r') - \sum_{m=1}^{m=n-1} P(m,r,\lambda_m)) \right] \quad (15)$$

a minimization routine generated the neighborhood distributions for both liquid- and gaslike samples; the results are in reasonable agreement with experiment, using  $G(r)$  as the initial (and solitary) input. Here the  $\lambda_n$  are parameters (one computed for each  $n$  value), while the  $a_n$  serve as normalization coefficients. It was found using the experimental database (nature's answer on how fluid  $G(r)$  can be partitioned) that the value of  $\lambda_n$  which minimizes quantity  $\Gamma_n$ , viz.

$$\Gamma_n = \int dr \left\{ \frac{(P(n,r,\lambda_n) - \frac{1}{2\pi r \rho})}{r^\beta} - \frac{(G(r) - \sum_{m=1}^{m=n-1} P(m,r,\lambda_m) - \frac{1}{2\pi r \rho})}{r^\beta} \right\}^2 \quad (16)$$

also aligns  $P(n,r,\lambda_n)$  with experimental  $P(n,r)$ . In other words, an indirect method can partition  $G(r)$  successfully and does not require specifics about the particle shape and potential. As with eqs 12 and 13, this method is applied sequentially to measured  $G(r)$ . The open squares in Figures 9 and 10 show results of applying this method. As one can see, the results offer substantial improvement over mathematical prescriptions for hard disks. In predicting first moments of  $P(n,r)$ , the agreement between calculated and experiment is especially striking for  $n$

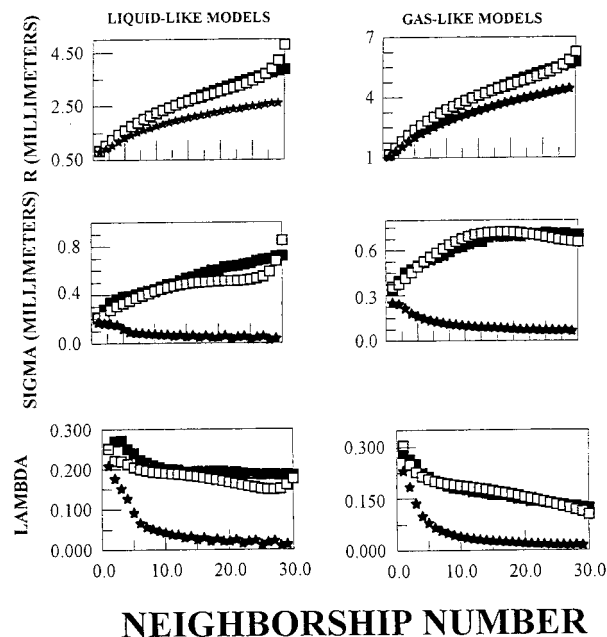


**Figure 10.** Experimental and calculated moment data. Filled squares, stars, and open squares denote experimental, hard disk, and indirect method results, respectively.

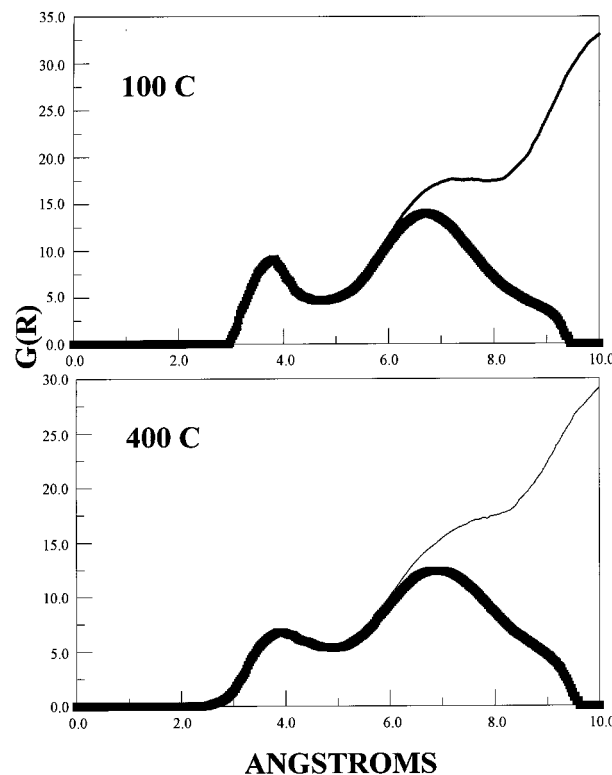


**Figure 11.** Radial distribution of liquid sodium atoms at 100 and 400 °C. Thin lines trace experimental  $G(r)$  reported in ref 17. Thick lines show the sum of the first 50 neighborhood distributions computed via the indirect method.

$< 20$ . Importantly, the indirect method works very well over an extended range of  $\beta$  values, namely 1–2.5.

## V. Discussion

A fluid's structure is given by the totality of correlation functions: singlet, pair, triplet, etc.,<sup>12</sup> the vast majority of which is unobtainable from lab experiments. Yet a case could be made that neighborhood distributions embedded in  $G(r)$  offer worthwhile and viable alternatives. This is where research here tries

to contribute, by examining  $G(r)$  and its partition attributes in a suitable model: an amalgam of wet lab experiments and computer image processing.

The results can address the questions posed in section I. First, via Figures 6–8 ( $P(n,r)$ , moment data, and overlap plots), one can explicitly compare fluid and crystalline structures. The outcome is that one finds only remote similarities between the two types of phase morphology. For the samples illustrated (and examined throughout this project), there is indeed only trace evidence of “staircase” behavior in  $\langle r_n \rangle$ -versus- $n$  data. Moreover, overlap plots such as in Figure 8 advance these comparisons a few steps further. The outcome is that the fluid samples evince shell structures bearing little resemblance to their crystalline counterparts.

While the results are confined to model systems, they are significant in the following sense. One view of fluids (especially liquids) is that of a “perturbed crystal”, such as in “hole” and lattice theories.<sup>13</sup> Accordingly,  $G(r)$  peaks represent the smeared residue of order in the solid state. While this view may be impossible to prove or disprove experimentally, it certainly seems a reasonable one. For example, there are many instances where  $G(r)$  for a crystal enables a good sketch of  $G(r)$  for the corresponding liquid.<sup>14</sup>

The present study cannot weigh the merits of hole and lattice theories. But our results do offer that a fluid’s shell structure need not mimic the corresponding crystalline phase at all. This follows from comparing A/D model structure with a regular hexagonal lattice. It is equally easy to draw comparisons between the model fluids and other crystalline lattice motifs; one is always led to the same interpretation. Note that the literature offers much discussion about fluid-versus-crystalline structure for monodisperse systems by way of computer simulations. One refers especially to work regarding the supercooling and crystallization properties of hard spheres.<sup>15</sup> By contrast, the tactic adopted in this paper has been an alternative, empirical one.

The model data foster comparisons between liquid and gas morphologies as well. The results are that one finds first moment scaling attributes of  $P(n,r)$  to be nearly identical for the two types of disordered samples. Also, the functionalities of the  $P(n,r)$  are very similar for liquid and gas models. This suggests that neighborhood distributions can be portrayed using very similar mathematical tools, regardless of the disordered phase particulars. In other words, the basic functionality of  $P(n,r)$  may transcend the specific phase (liquid or gas) under consideration.

There are notable differences in the neighborhood partition structures of liquid- and gaslike samples. For example,  $P(n,r)$  for the two different phases demonstrate disparate signatures by way of  $\Lambda_n$ -versus- $n$ . The maximum in  $\Lambda_n$  always occur at  $n = 1$  for the gaslike samples; by contrast, a maximum in  $\Lambda_n$  at  $n = 4$ –5 is a distinct marker for the liquid morphology. Different signatures are also found in the overlap plots for liquid- and gaslike samples, although here the distinctions (e.g. in Figure 7) can be very subtle. The smear patterns best distinguish the two phase morphologies when viewed along the diagonal elements.

The different phase signatures contained in  $\Lambda_n$  and  $O_{n,r'}$  are also significant. Liquids and gases are both types of “disordered” systems. As such, there are few markers (at least at the atomic scale) which can distinguish one type of sample from the other. As is well-known, the extent of hills and valleys in  $G(r)$  and  $g(r)$  is one telltale marker.<sup>16</sup> Yet by the model, one sees that the two phase morphologies may also be recognized

by the functionality of  $\Lambda_n$ -versus- $n$  and (to a lesser degree) the contour-fill plots ( $O_{n,r'}$ ) such as in Figure 7.

The results also offer comparisons (Figures 9 and 10) between experimental data and theory for hard disks (section II). These comparisons show how sensitive predictions of  $P(n,r)$  can be to particle shape and potential approximations. It follows that analytical attempts to partition  $G(r)$  can be way off nature’s mark, given uncertainties in excluded and free volume structure. Fortunately, one finds that  $G(r)$  can be unraveled to yield  $P(n,r)$  without specific reference to particle shapes and potentials. It may then be the case that analogous techniques are effective for real atomic systems. Note that in arriving at the indirect method computed  $P(n,r)$  could always be “checked” with experiment’s (nature’s) answer. Labwork with real atomic fluids does not permit this venture.

Success of the indirect method has motivated several applications to atomic systems. Figures 11–14 offer sample results based on  $G(r)$  obtained via X-ray scattering for liquid sodium at 100 and 400 °C.<sup>17</sup> In constructing these results, eq 15 was used in basically the same parametrized form:

$$P(n,r,\lambda_n) = a_n(G(r) - \sum_{m=1}^{m=n-1} P(m,r,\lambda_m)) \times \exp[-\lambda_n \int_0^r dr' (G(r') - \sum_{m=1}^{m=n-1} P(m,r,\lambda_m))] \quad (17)$$

However, the radial distance  $r$  was specified by three polar (or Cartesian) coordinates instead of two. Accordingly, eq 16 was adapted to the case of three dimensions, namely

$$\Gamma_n = \int dr \left\{ \frac{(P(n,r,\lambda_n) - 1)}{4\pi r^2 \rho} - \frac{(G(r) - \sum_{m=1}^{m=n-1} P(m,r,\lambda_m))}{4\pi r^2 \rho} \frac{1}{r^\beta} \right\}^2 \quad (18)$$

By analogy with the model study, parameters  $\lambda_n$  were computed sequentially so as to minimize the integral in eq 18. In the calculations,  $\beta$  was taken to be unity (as in the vast majority of A/D model studies), while the  $a_n$  again served as normalization coefficients.  $G(r)$  was obtained by applying third-order spline functions to data optically scanned from ref 17. The proposal here is that computed  $P(n,r,\lambda_n)$  (Figure 12) are facsimiles of the neighborhood distributions embedded in sodium  $G(r)$ . It is unfortunate that these cannot be checked by lab experiment. Nonetheless the calculations are easy to perform and portray liquid sodium at new levels of structural detail.

The computed structures warrant a few comments. Figure 11 shows experimental  $G(r)$  (thin lines<sup>17</sup>) along with the sum of computed neighborhood distributions (thick lines),  $n = 1, 2, \dots, 50$ . Figure 12 then illustrates computed  $P(n,r)$ , all observed to be single-modal. Not surprisingly, one finds the  $P(n,r)$  widths to be greater for the higher temperature liquid. For both high- and low-temperature samples, the neighborhood distributions overlap over an extended range of  $n$  values. This is especially appreciated when using thick lines (as in Figure 13) to graph  $P(n,r)$ ; one finds the neighborhood distributions to form a near-continuum at ca.  $n = 16$ –20.

Figure 13 illustrates moment calculation results for liquid sodium  $P(n,r)$ . The top panel includes  $\langle r_n \rangle$  appropriate to a body center cubic lattice, the structure of sodium crystal.<sup>18</sup> Unlike the model structure data, the results suggest formal similarities between the liquid and crystalline structures, even at tempera-

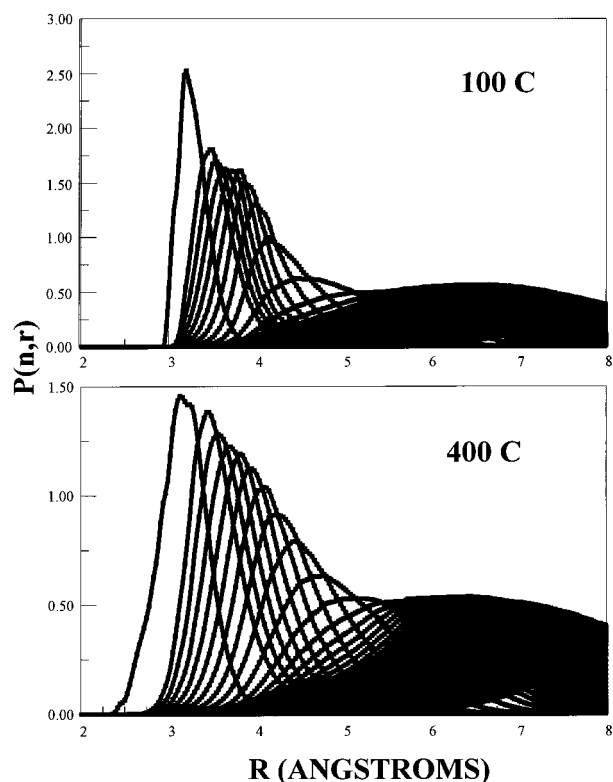


**Figure 12.** Neighborhood distributions calculated for liquid sodium. Upper and lower panels illustrate  $P(n,r)$ ,  $n = 1, 2, \dots, 50$  computed for  $G(r)$  of Figure 11.

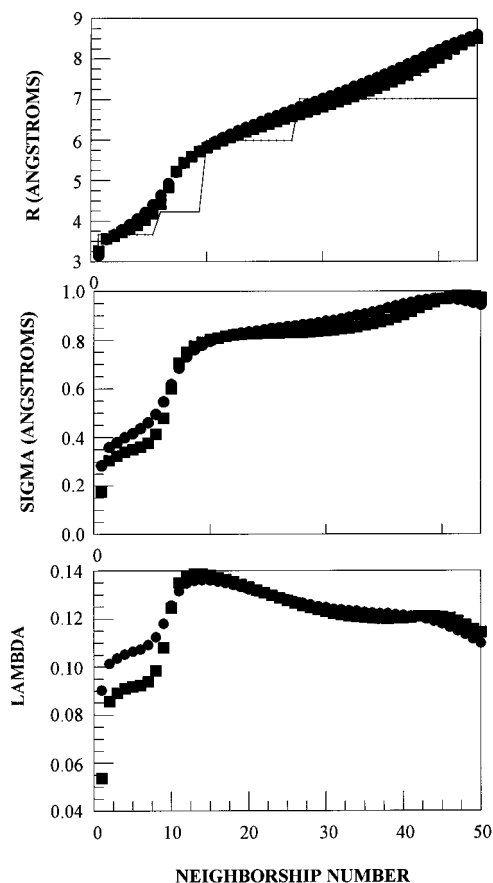


**Figure 13.** Moment calculations for liquid sodium. The top panel includes  $\langle r_n \rangle$  appropriate to the bcc structure of sodium crystal. 100 and 400 °C data are denoted by filled squares and circles, respectively.

tures significantly above the freezing point. The  $\Sigma_n$  demonstrate slight clefts near  $n = 16$  for both low- and high-temperature

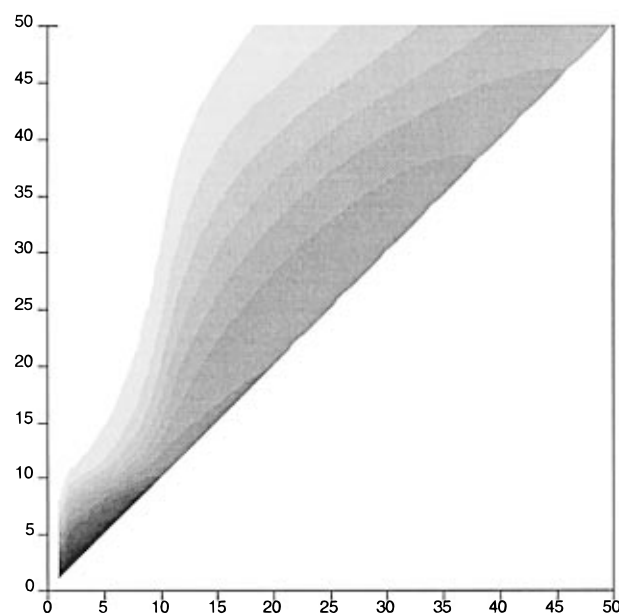
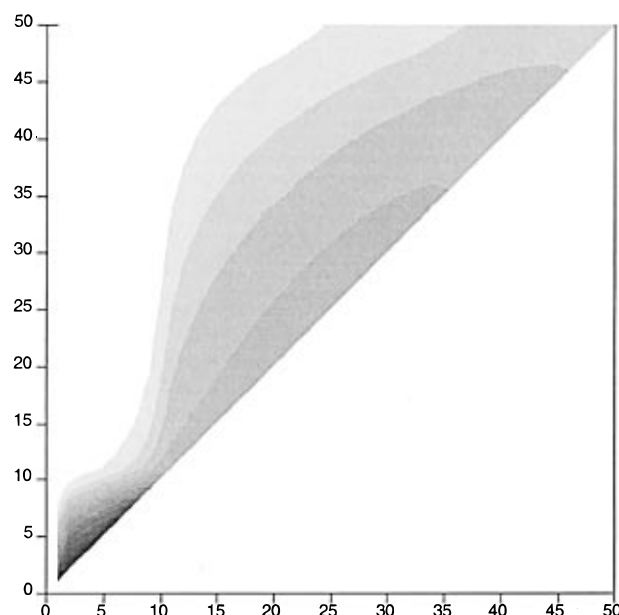


**Figure 14.** Overlap contour-fill plots for liquid sodium. The blackness in each slot of the upper triangular arrays is proportional to the overlap integrals (eq 14) computed via the indirect method results.

cases. For  $\Lambda_n$ -versus- $n$ , the observed signatures are consistent with a liquid morphology, as in the model studies. For both 100 and 400 °C sodium, the maximum in  $\Lambda_n$  occurs near  $n = 12$ . Figure 14 illustrates computed  $P(n,r)$  overlap characteristics for liquid sodium by way of contour-fill plots. There appear to be only subtle differences in the “smear” patterns at the two different temperatures.

## VI. Summary and Closing Remarks

Fluid structure has been examined in additional detail using foam image models. In so doing, one observes essential characteristics of  $P(n,r)$  and relation to  $G(r)$ . The model experiments offer a basis for addressing section I questions. Likewise, an indirect method for partitioning  $G(r)$  was offered, owing to the luxuries of comparing computed and experimental  $P(n,r)$  and theory of previous researchers.



This study was made possible by combined wet lab work and computer image processing. Naturally, there are further questions to address, for example, what symmetry elements are lost in what order as a crystal melts? Nature hides the answer to this question at the atomic level, so additional application is being made of detergent foam models.

**Acknowledgment.** The authors are grateful to Drs. James Glazier and D. Udler for informative reprint materials and discussions. Support from the Department of Chemistry at Loyola University of Chicago and technical assistance of J. E. Graham and Joseph Brunzelle are further appreciated. The comments and criticism of Professor Willetta Greene-Johnson and an anonymous reviewer are appreciated.

## References and Notes

- (1) See, for example: Chen, S.-H. In *Structure of Liquids in Physical Chemistry, An Advanced Treatise*; Henderson, D., Ed.; Academic: New York, 1971; Vol. VIIIA, Chapter 2.
- (2) See, for example: Gingrich, N. S. *Rev. Mod. Phys.* **1943**, *15*, 90.
- (3) See, for example: Andersen, H. C.; Chandler, D.; Weeks, J. D. *Adv. Chem. Phys.* **1976**, *105*.
- (4) Barker, J. A.; Henderson, D. *Rev. Mod. Phys.* **1976**, *48*, 587. Egelstaff, P. A. *An Introduction to the Liquid State*; Academic: New York, 1967. Hansen, J. P.; McDonald, I. R. *Theory of Simple Liquids*; Academic: London, 1976.
- (5) See, for example: Doye, J. P. K.; Wales, D. J. *Science* **1996**, *271*, 484. Hecht, C. E. *Statistical Thermodynamics and Kinetic Theory*; Freeman: New York, 1990; Chapter 3.
- (6) Graham, D. J.; Magdalinis, P.; Pimentel, D. *J. Phys. Chem. B* **1997**, *101*, 11204.
- (7) Hertz, P. *Math. Ann.* **1909**, *67*, 387.
- (8) Reiss, H.; Frisch, H. L.; Lebowitz, J. L. *J. Chem. Phys.* **1959**, *31*, 369.
- (9) Torquato, S.; Lu, B.; Rubinstein, J. R. *Phys. Rev. A* **1990**, *41*, 2059. Torquato, S.; Lee, S. B. *Physica A* **1990**, *16*, 361.
- (10) MacDonald, J. R. *J. Phys. Chem.* **1992**, *96*, 3861.
- (11) Bragg, L.; Nye, J. F. *Proc. R. Soc. London* **1947**, *A190*, 474.
- (12) Blum, L. Narten, A. H. *Adv. Chem. Phys.* **1976**, *203*.
- (13) Hill, T. L. *Introduction to Statistical Thermodynamics*; Dover: New York, 1986; Chapter 17.
- (14) See, for example: J. D. Bernal, *Nature (London)* **1959**, *183*, 141; **1960**, *185*, 68; *Proc. R. Soc. London* **1964**, *280*, 299.
- (15) See, for example: Qi, D. W.; Lu, J.; Wang, S. *J. Chem. Phys.* **1992**, *96*, 513. Hsu, C. S.; Rahman, A. *J. Chem. Phys.* **1979**, *70*, 5234. Cape, J. N.; Finney, J. L.; Woodcock, L. *J. Chem. Phys.* **1981**, *75*, 2366. Yang, J. X.; Gould, H.; Klein, W.; Mountain, R. D. *J. Chem. Phys.* **1990**, *93*, 711.
- (16) Goodstein, D. L. *States of Matter*; Dover: New York, 1985; Chapter 4.
- (17) Trimble, F. H.; Gingrich, N. S. *Phys. Rev.* **1938**, *53*, 278.
- (18) Ashcroft, N. W.; Mermin, N. D. *Solid State Physics*; Saunders College: Philadelphia, 1976.